LASER & PHOTONICS REVIEWS
www.lpr-journal.org

Multichannel Linear and Nonlinear Information Encryptions with Malus Metasurfaces

Yuexin Sun, Guangzhou Geng, Yanchun Wang, Yuebian Zhang, Zhancheng Li, Wenwei Liu, Hua Cheng,* and Shuqi Chen**

The superior capability of wavefront manipulation makes metasurfaces a promising platform for implementing high-density information storage and multifold optical encryption. Although some metasurfaces have realized information encryption, it is still challenging to implement polarization-encrypted grayscale images in both linear and nonlinear channels. Here, a novel approach to realize multichannel linear and nonlinear information encryptions is proposed based on nonlinear Malus metasurfaces composed of single-sized meta-atoms, in which the polarization states of the linear and nonlinear signals can be decoupled. As a proof of concept, two distinct grayscale images with different polarizations have been encrypted in the fundamental and second harmonic wave channels simultaneously. Besides, by further introducing the nonlinear Pancharatnam-Berry phase, a tri-channel polarization encrypted metasurface with a multi-level grayscale image in the near field and two holographic images in the far field has been experimentally demonstrated at the second harmonic frequency. This work provides more degrees of freedom for multichannel information storage and opens an avenue for optical information encryption in both linear and nonlinear regimes.

1. Introduction

Metasurfaces composed of artificial subwavelength structures have garnered much interest for their excellent wavefront manipulation ability. By tailoring the constituent material, shape, and the rotation angle of meta-atoms of the metasurface, various fascinating phenomena, including anomalous refraction,[1–3] vortex beam generation,[4–7] holography display[8,9] and optical imaging[10,11] have been realized. Recently, metasurfaces featuring multiple information channels have been proposed to address the pressing demands for vast information storage capacity, enhanced device integration compatibility, and high-security optical encryption. For example, synthetically color images,[12–15] angular-multiplexing,[16,17] polarization-dependent nanoprintings[18–23] have been implemented with multichannel metasurfaces. In particular, attaching multiple information to different polarization channels has aroused wide concern. These multichannel applications are commonly implemented by few-layer[24,25] or polyatomic[26,27] metasurfaces, which require complex sample fabrication processes. Due to the orientation degeneracy and continuous amplitude modulation of Malus's law, Malus metasurfaces are capable of encoding versatile information into multiple different channels using only single-sized structures, dramatically simplifying the fabrication process and reducing the crosstalk between different channels.[28,29] They have attracted extensive attention and displayed superior multichannel polarization manipulation capacity.[30–33] However, most multichannel Malus metasurfaces only work at a single frequency, which severely hinders the improvement of information capacity and device integration.

Recent studies in metasurfaces reveal their potential ability in nonlinear frequency conversions and nonlinear signal manipulations,[34–50] providing a new strategy for frequency multiplexing. The phase-matching condition of the nonlinear process is released in metasurfaces because of their nanoscale dimension. Furthermore, numerous nonlinear wavefront manipulations have been achieved, such as nonlinear holograms,[35,36,38,51] nonlinear optical vortexes,[5,52] and nonlinear metalenses.[53,54] Benefiting from the simple relationship between the phase and the rotation angle of structures, the nonlinear Pancharatnam-Berry (PB) phase has been extensively employed in engineering the wavefront of nonlinear signals.[35,37] Nonlinear multichannel optical information multiplexing has also been successfully

Y. Sun, G. Geng, Y. Wang, Y. Zhang, Z. Li, W. Liu, H. Cheng, S. Chen
The Key Laboratory of Weak Light Nonlinear Photonics, Ministry of Education, School of Physics and TEDA Institute of Applied Physics
Nankai University
Tianjin 300071, China
E-mail: ybzhang@nankai.edu.cn; hcheng@nankai.edu.cn; schen@nankai.edu.cn

S. Chen
School of Materials Science and Engineering, Smart Sensing Interdisciplinary Science Center
Nankai University
Tianjin 300350, China

S. Chen
The Collaborative Innovation Center of Extreme Optics
Shanxi University
Taiyuan, Shanxi 030006, China

The ORCID identification number(s) for the author(s) of this article can be found under https://doi.org/10.1002/lpor.202300866

DOI: 10.1002/lpor.202300866

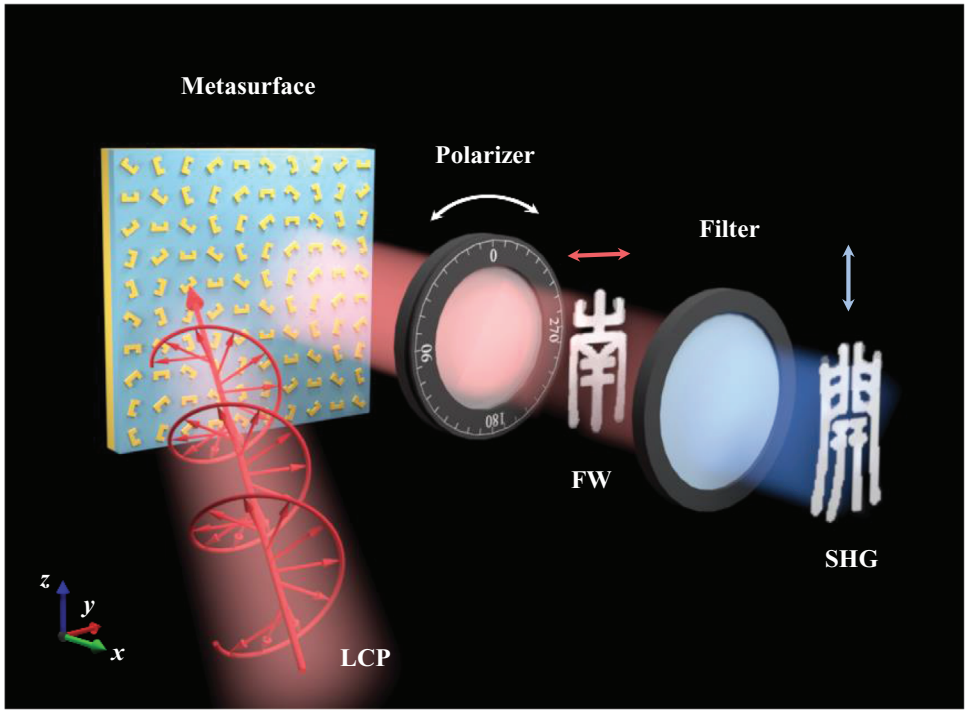

Figure 1. Schematic of the Malus metasurface for linear and nonlinear information encryption. Under the pumping of the LCP fundamental wave (FW), the plasmonic metasurface can generate the fundamental and SH signals simultaneously. A polarizer is inserted at the reflection path to decode grayscale images of different channels, and a filter is utilized to display the image at the SH frequency.

implemented in previous publications.[52,55] Moreover, optical information can be constructed in both linear and nonlinear regimes simultaneously, providing new possibilities for information encryption.[5] By expanding the PB phase and Malus's law to nonlinear optical regimes, different optical information can be encrypted into different frequency or polarization channels.[56] Generally, due to the strong enhancement of the electromagnetic field at the fundamental resonance, the manipulation of nonlinear signals is always performed under the resonance condition to obtain the maximum conversion efficiency. However, the polarization states of linear and nonlinear signals generated at resonant wavelengths are always related to each other and cannot be manipulated independently. For example, for split-ring resonators (SRRs), the polarization of the fundamental wave is usually perpendicular to the second harmonic (SH) polarization under horizontally polarized incidence.[57] As a result, the hidden grayscale image in the nonlinear channel can be inferred and distinguished through the fundamental wave channel, thus invalidating the encryption ability of the nonlinear channel. Furthermore, in order to fully exploit the encryption potential of nonlinear metasurfaces and enhance information confidentiality, more information channels should be explored for cooperative concealment.

Here, we demonstrate the nonlinear Malus metasurfaces with single-sized SRRs that can realize the polarization decoupling of the fundamental and SH waves. Different optical information can be encrypted into different frequency channels with negligible crosstalk, significantly improving information security. To experimentally demonstrate the capability of this method in multichannel information storage and multifold optical encryption, we encoded two polarization-dependent grayscale images in two frequency channels based on Malus's law. This polarization decoupled method has greater potential in realizing information hiding and multifold anti-counterfeiting. To further extend the number of information channels, we realized the encryption of distinct images in different polarization states of the SH wave in near and far fields. The proposed nonlinear Malus metasurfaces can provide more channels for information storage and significantly improve the confidentiality of encrypted data, which may provide a further step in the development of optical communication and encryption devices.

2. Results and Discussion

Figure 1 schematically illustrates the novel design scheme of the multichannel polarization encryption metasurface, which can realize polarization decoupling of the fundamental and SH wave channels. Two independent grayscale images displayed in two frequency channels are constructed in a single Malus metasurface with uniform structures. When illuminating the designed metasurface with a left-handed circularly polarized (LCP) fundamental wave, a grayscale image of the Chinese character "nan" can be decrypted by a polarizer with its transmission axis horizontally oriented. Another Chinese character "kai" can be revealed by inserting a filter into the optical path to filter out the fundamental wave and rotating the transmission axis of the polarizer to the vertical direction.

To achieve multichannel polarization encryption, we adopt SRRs as the building blocks of Malus metasurfaces. The SRRs with onefold (C_1) rotation symmetry in shape have been widely

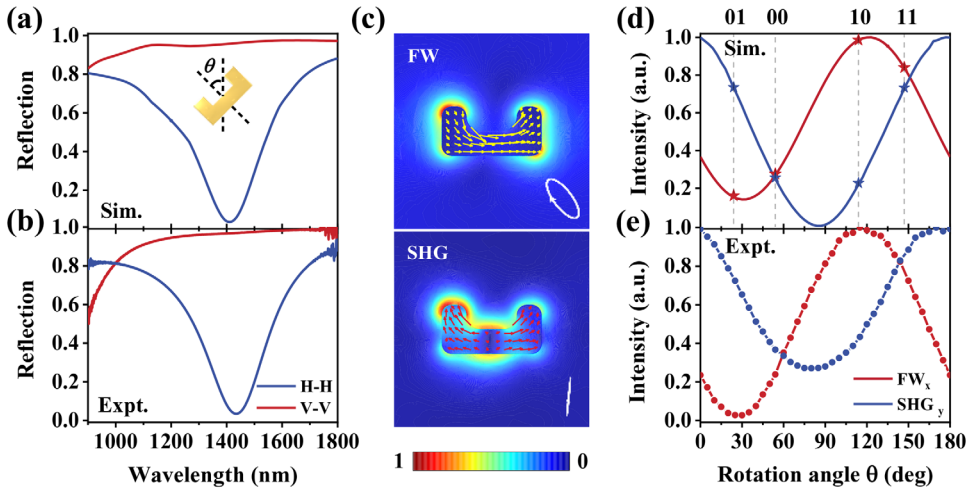

Figure 2. Working principle of the SRR and design principle of the Malus metasurface. a) Simulated and b) measured reflection spectra for linear polarization incidence. The resonant wavelength is ≈1400 nm in both the simulated and measured results. The inset shows the top view of the SRR with rotation angle θ. The long arm length L_x is 204 nm, the short arm length L_y is 100 nm, the arm width w is 50 nm, and the thickness t is 30 nm. c) Calculated surface current densities for the fundamental wave (yellow arrows) and SH wave (pink arrows) channels under LCP pumping. The color maps show the electric field distributions at different frequency channels. The polarization ellipses of different channels are depicted in the inset. d) Simulated and e) measured intensities of the fundamental wave (red lines) and SH wave (blue lines) as functions of the rotation angle when the polarization of the fundamental wave is LCP. The gray dashed lines indicate four rotation angles used to encode grayscale images. The corresponding intensities in the fundamental wave (red stars) and SH wave (blue stars) channels are "01," "00," "10," and "11".

used in boosting nonlinear conversion efficiency and manipulating nonlinear polarization states due to their resonance properties.[46–48] The inset of **Figure 2a** shows the top view of the proposed gold SRR located on the photoresist (SU8) spacer layer, with a gold mirror layer at the bottom to form the metal-insulator-metal (MIM) nanocavity. The electromagnetic field of the fundamental wave can be strongly confined in the MIM nanocavity, inducing enhancement of light-matter interaction. The period of the unit cell p is 400 nm. The optimized SRRs are described by the long arm length L_x, the short arm length L_y, the width w, and the thickness t. The thicknesses of the SU8 spacer and the gold reflector layers are 88 and 90 nm, respectively. All numerical simulations were performed by the finite element method with the commercial software COMSOL Multiphysics. A metasurface composed of SRRs with uniform orientations is used to explore the resonance and polarization properties of SRRs at different frequencies. The periodic boundary conditions are applied in the x and y directions, and perfectly matched layers are imposed along the z direction. The metasurface is illuminated by the linearly polarized fundamental wave along the -z direction. The permittivity of gold was obtained from Palik's handbook,[58] and the refractive index of SU8 was taken as 1.53. Figure 2a shows the simulated reflection spectra of the periodically arranged SRRs with the incident polarization parallel (blue line) or perpendicular (red line) to the base of the SRR. Intuitively, the incident electric field couples to SRRs when the incident polarization is along the base of the SRR, and a magnetic dipole mode is excited at 1400 nm, corresponding to a dip in the reflection spectra. However, the magnetic resonance vanishes for vertically polarized incident light. The measured reflection spectra displayed in Figure 2b were captured by a Bruker VERTEX 70 Fourier transform infrared spectrometer. The experimental results are in good agreement with the simulations. We calculated the reflection spectra and the corresponding SH signal with different wavelengths under LCP incidence (Figure S1, Supporting Information). The nonlinear harmonic responses were calculated by employing the hydrodynamic model.[43,57] The strongest second harmonic generation (SHG) response is observed ≈700 nm, which is half of the fundamental resonant wavelength. We also calculated the SH conversion efficiency $\eta = P_{av}^{SH}/P_{av}^{FW} \approx 2.63 \times 10^{-10}$ for an average pump intensity of 55 MW cm^{-2} at the fundamental wavelength of 1550 nm, which is at the same level as previous reports.[44,57]

To realize polarization decoupling of two frequency channels, we choose the off-resonant wavelength 1550 nm as the pump wavelength. The surface current distributions and polarization ellipses under the pumping of the LCP fundamental wave are calculated to investigate the polarization states at different frequency channels. The polarization ellipse is characterized by two angles: the direction of the major axis ψ and the ellipticity χ of the polarization ellipse, which can be attained and expressed as

$$\tan 2\psi = \frac{2R}{1-R^2}\cos\varphi, \tag{1}$$

$$\sin 2\chi = \frac{2R}{1+R^2}\sin\varphi, \tag{2}$$

where $R = a_y/a_x$ is the ratio of the amplitude of the x and y components of the output electric field. $\varphi = \varphi_y - \varphi_x$ is the phase difference of the electric fields. As shown in Figure 2c, circulating currents at the fundamental wave correspond to the existence of a magnetic dipole mode, and the generated SH surface currents are almost perpendicular to the base of SRRs. The inset of Figure 2c presents the polarization ellipses of the two frequency channels, which reveals the polarization state of the fundamental wave is elliptical, while the SH polarization is almost linear and

along the vertical direction. The presence of an angle between the major axes of the polarization ellipses in both channels is apparent, suggesting that the intensity curves of the reflection waves in two channels are interleaved, thereby facilitating independent intensity manipulation of the fundamental and SH wave channels. In fact, the major axis direction of the polarization ellipse of the fundamental wave can be significantly changed while keeping that of the SH wave basically unchanged at the off-resonant condition (see Figure S2a, Supporting Information). That is to say, the polarization states of the two channels can be independently manipulated in a specific range by adjusting the detuning between the working wavelength and the resonant wavelength. Meanwhile, the major axis direction of the polarization ellipse varies with the rotation angle of the structure, and the ellipticity remains unchanged (see Figure S2b, Supporting Information), which ensures the applicability of Malus's law.

Based on the different polarization states of the two frequency channels and Malus's law, the output intensities for the two frequency channels can be decoupled. The x-polarization intensity of the fundamental wave channel and the y-polarization intensity of the SH wave channel under LCP incidence are plotted as functions of the rotation angle in Figure 2d. The component intensities can be defined as cosine functions of the major axis direction (ψ), which varies with the rotation angle (θ) of SRRs. These two cosine functions have different trends, so four states of "01," "00," "10," and "11" of two different channels can be achieved naturally by selecting four structures with different orientation angles, where "0" and "1" represent low and high intensity states, respectively. Each unit cell participates in the imaging of two frequency channels. On the basis of these four states, different optical information attached to different frequency channels can be recorded into the orientation angle of SRRs. Figure 2e shows the experimental results of Malus's law extracted by integrating designated parts of the images taken by the specific camera. Even though the minimum values of intensities are slightly different due to the ambient noise, the fabrication and measurement imperfections, the measured curves have the same tendency as the designed ones. (More details about the dependence of the polarization state of the fundamental wave channel on the fabrication errors can be found in Figure S3 in the Supporting Information.)

To vividly illustrate the encryption ability of the proposed method, we encoded two polarization-dependent grayscale images in two frequency channels. The designed nonlinear Malus metasurfaces were fabricated by standard electron-beam lithography (EBL) and lift-off process. **Figure 3**a shows the scanning electron microscopy (SEM) image of a portion of the sample, in which different colors represent different orientation angles of the unit cell. Four basic rotation angles represented by different colors are consistent with the angles marked by gray dashed lines in Figure 2d, which induce distinctive intensity distributions on two frequency channels. The reflection intensity values of the four basic structures composing the metasurface in the two frequency channels can be represented by binary code states, as shown in Figure 3b. The two grayscale images generated by the fabricated Malus metasurface can be selectively read out by choosing specific frequency channels in the experimental setup shown in Figure 3c. Figure 3d and e exhibit the simulated results of the grayscale images in the fundamental and SH channels, respectively. The transmission axes of the polarizers are indicated by the white arrows in the upper left corner of the images. For the fundamental wave channel, the Chinese character "nan" can only be decoded when the transmission axis of the polarizer is rotated to the x direction. Another Chinese character "kai" can be captured at the SH wave channel by inserting a filter into the optical path and rotating the transmission axis of the polarizer to the orthogonal direction. Crosstalk exists in the image of the fundamental wave channel, indicating that the intensity of the fundamental channel deviates slightly from the ideal binary grayscale, which can be seen from Figure 2d, where the intensities marked by red stars correspond to four gradients. However, the SH wave channel with binary intensity marked by blue stars has negligible crosstalk. The corresponding experimentally measured images in Figure 3f and g agree well with the simulated results.

The aforementioned nonlinear Malus metasurface only encrypts two-level grayscale images on two channels. To explore more degrees of freedom for information storage and encryption, we demonstrate a tri-channel information encryption metasurface at the SH frequency by combining the nonlinear PB phase and Malus's law, which can encrypt a grayscale image in the near field and project two holographic images in the far field simultaneously, as shown in **Figure 4**a. Additionally, the grayscale image exhibits six gray levels, increasing the capacity of information encryption. The reflection spectra and the SH intensity of the proposed Malus metasurface are calculated in Figure S4 (Supporting Information). The magnetic resonance is ≈1550 nm, where the maximum intensity of the SH signal appears. The phase profile of the metasurface is divided into two sections to realize the multiplexing of three channels, as shown in Figure 4b. The inner part, consisting of structures with six orientation angles, is used to encrypt a multi-level grayscale image in the near field based on Malus's law. The surrounding part, with orientation angles ranging from 0 to π, is calculated by the modified Gerchberg–Saxton algorithm (Figure S5, Supporting Information) to generate holographic images. Notably, this segmented configuration can further integrate frequency and spatial dimensions by encoding the grayscale image of the fundamental wave channel into the inner part. Based on the principle of the nonlinear PB phase, the relation between the rotation angle θ and the geometric phase φ of the SH wave satisfies $\varphi = \sigma\theta$ for the wave with the same polarization (σ) as that of the fundamental wave, and for the opposite polarization (-σ), $\varphi = 3\sigma\theta$ (see Figure S6, Supporting Information). Thus, the orientation distribution of meta-atoms can be derived from the phase profile. Figure 4c depicts the SEM image of the fabricated sample with the orientation angles of the structures distributed randomly from 0 to π.

Two holograms can be clearly reconstructed in the far field under normal incidence of LCP fundamental wave. As shown in Figure 4d and e, the letter "N" can be decrypted in the far field if the output polarization is filtered to the right-handed circularly polarized (RCP) state, while the letter "K" is decrypted when the output polarization is reversed to the LCP state. Furthermore, a multi-level grayscale image can be simultaneously decrypted in the near field by a polarizer whose transmission axis is along the x-axis. A clear flower with five petals of different grayscales is decoded in the near field, as shown in Figure 4f. Figure 4g–i display the corresponding experimentally measured images,

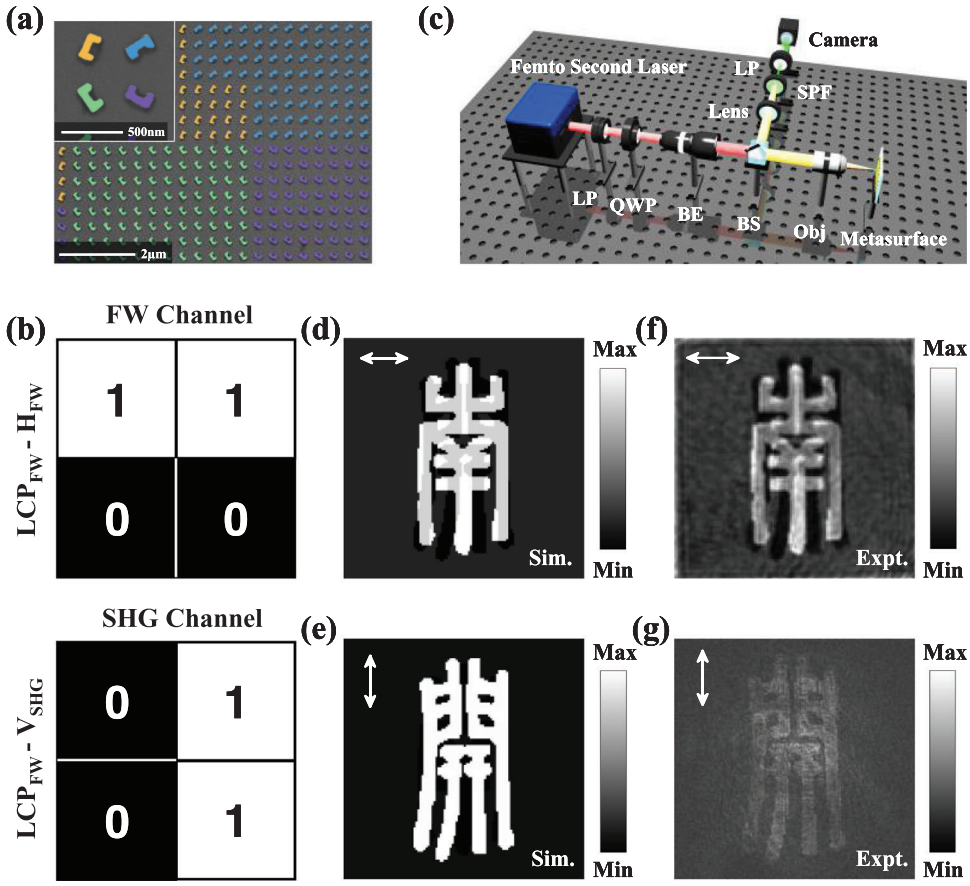

Figure 3. Linear and nonlinear information encryption with the Malus metasurface. a) Partial SEM image of the fabricated metasurface. Different colors indicate structures with different orientation angles. The inset shows four meta-atoms utilized to encode grayscale images. b) Binary intensity code states of the fundamental and SH wave channels corresponding to the structures shown in the inset of (a). c) Schematic of the experimental setup. LP, linear polarizer; QWP, quarter-wave plate; BE, beam expander; BS, beam splitter; Obj, objective; SPF, short-pass filter. Simulated grayscale images of the d) fundamental wave and e) SH wave channels. f-g) Corresponding measured results of the images shown in d) and e). The white arrows in d–g) indicate the transmission axes of the polarizers.

with the edges marked by blue dotted lines for visualization. It can be intuitively seen that the two polarization channels of holography are independent. The slight discrepancy between the simulated and measured results mainly arises from the deviation of polarizations in the experiment. The variation of gray levels can be clearly seen in the magnified view of the experimentally captured near-field image in Figure 4i. The intensity distribution of the surrounding area used to encode holograms is messy due to their arbitrary rotation angle distribution. To more intuitively illustrate the results, we evaluate the intensity of each petal. The designed orientation angles (θ) of the five petals are 21°, 36°, 51°, 66°, and 81°, respectively, and the corresponding intensities are indicated by blue stars in Figure 4j. In addition, we chose the structure with the rotation angle of 0° as the constituent unit of the inner black background, so that the flower can stand out from the surrounding environment. The gradual variation trends of grayscales can be perspicuously distinguished only by inserting a polarizer into the optical path with its transmission axis aligned along the x-axis. There will be an inverse intensity distribution when the polarizer is rotated to the vertical orientation, whereas the distribution of gray levels will be irregular and unclear when the transmission axis of the polarizer is in other directions. Figure 4k presents the integrated intensity of each petal captured from experiments. Five gray levels can be unambiguously seen, and the relative brightness between different petals is consistent with the simulated results, which validates the capability of the nonlinear Malus metasurface to encode multi-level grayscale images. The variation of intensities is more noteworthy than specific values of the intensities, so although the absolute values of the experimental intensities are different from the simulations, it does not affect the description of the primary function.

3. Conclusions and Outlook

In conclusion, we theoretically proposed and experimentally verified multichannel linear and nonlinear information encryption by nonlinear Malus metasurfaces. The polarization states of the fundamental and SH frequencies can be decoupled at the off-resonant wavelength. Two different polarization-encrypted images can be encoded in two frequency channels independently. The corresponding grayscale images can only be distinctly ob-

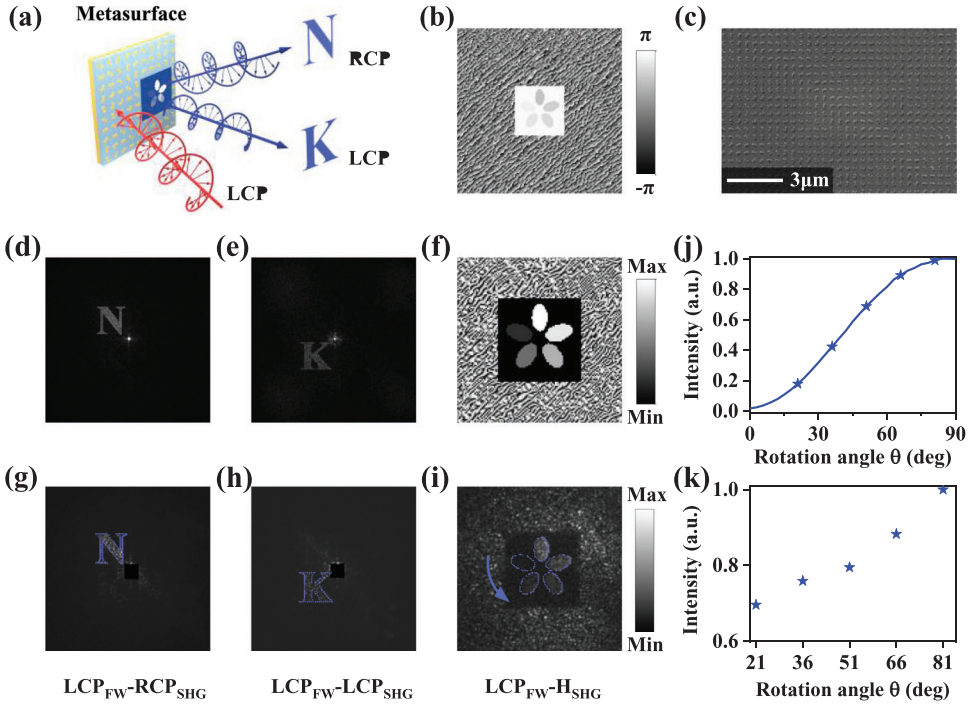

Figure 4. Tri-channel information encryption at the SH frequency. a) Schematic of the tri-channel metasurface to realize the near-field grayscale image and far-field holograms. The generated LCP SH wave encodes a holographic image of "N," and the SH signal with RCP encodes a holographic image of "K" under LCP fundamental wave incidence. Furthermore, there is a multilevel grayscale image in the near field. b) The phase distribution of the metasurface to encode near- and far-field images. c) Partial SEM of the fabricated metasurface. Simulated holographic images of the d) RCP and e) LCP SH waves. f) The simulated grayscale image of the SH channel when the polarizer transmission axis is along the *x*-axis. g–i) Corresponding measured results of the images shown in d–f). The blue dotted lines outline the edges of the characters. The blue arrow in (i) indicates the change in petal brightness from dark to light. j) The intensity of the generated SH wave is a cosine function of the orientation angle. The grayscale of petals in f) corresponds to intensities marked by blue stars, and the rotation angles are 21°, 36°, 51°, 66°, and 81°, respectively. k) Intensities of five petals extracted from the experimentally captured image.

served at a particular output polarization and frequency. To introduce more degrees of freedom, we realized the multi-level grayscale image in the near field and two holographic images in the far field at the SH frequency. The number of information channels can be further increased if we replace the inner part of the metasurface with structures that can produce binary grayscale images in two frequency channels. Based on nonlinear Malus metasurfaces, encoding the continuous and binary grayscale images on two frequency channels can also be simultaneously achieved. (More details can be found in S7 in the Supporting Information.) Compared with previous multichannel metasurfaces, the proposed metasurfaces expand the frequency channel for information encryption and realize multi-polarization encryption on the SH wave channel. By subtly manipulating the phase profile of the metasurfaces, more intriguing applications can be realized. Moreover, different information dimensions can be incorporated to empower encryption. For instance, by dividing target information into multiple segments and encrypting them into different channels, such as linear/nonlinear, near/far-field, and linear/circular polarization, the confidentiality of information can be significantly improved. Our proposed metasurfaces provide strategies for more sophisticated multichannel information encryption, and may also be extended to high-density optical storage and multi-frequency information multiplexing.

4. Experimental Section

Sample Fabrication: Metasurfaces were fabricated using standard EBL and lift-off process. First, a 90 nm gold reflector layer was deposited on the fused silica substrate by the electron beam deposition (EBD) method. An 88 nm SU8 resist was subsequently coated and reinforced by ultraviolet light. Then, a layer of poly (methyl methacrylate) (PMMA) with a thickness of 120 nm was spun coated on the substrate. After that, a layer of poly(3,4-ethylenedioxythiophene) polystyrene sulfonate (PEDOT:PSS) with a thickness of 35 nm was spun coated to eliminate the charging effect during the EBL process, employing a 100 kV voltage, 200 pA current and 1100 μC cm^{-2} dose. After defining the patterns of the designed metasurfaces by the EBL process, the PEDOT:PSS layer was removed by pure water for 60 s, and PMMA resist was developed with methyl isobutyl ketone (MIBK)/ isopropyl alcohol (IPA) (1:3) for 40 s. Afterward, a 2 nm Cr layer and a 30 nm gold layer were deposited on the sample with the EBD method. Here, the function of the Cr layer was to enhance the adhesion between the structures and the SU8 layer. Finally, residual parts out of patterns were stripped by removing PMMA with hot acetone at the temperature of 60 °C for 20 min during the final lift-off procedure, leaving the SRRs on the substrate.

Experimental Procedure: An erbium-doped ultrafast fiber laser (Toptica Photonics AG FemtoFiber Pro NIR, repetition frequency: 80 MHz, pulse length: ≈80 fs) centered at 1550 nm was utilized as the incident fundamental wave coupled to the home-built microscope. A linear polarizer (LP) and a quarter-wave plate (QWP) were used to generate the incident LCP light. Then, the incident beam was expanded with a beam expander (BE) to illuminate the entire sample. The input beam is incident normally on the

metasurface. Another LP and QWP were inserted to filter the linear and nonlinear signals with a certain polarization state, and different frequency channels were selected by a filter (SPF). The generated linear and nonlinear images were deflected by a beam splitter (BS) and then captured with an objective, a lens, and a camera. For linear measurement, the average power of the fundamental wave was 350 mW, and the generated images were collected by a 20 × objective (SIGMA-KOKI PAL-20-NIR-HR-LC00 20 × NA = 0.45), a lens (f = 150 mm), and an InGaAs camera (HAMAMATSU InGaAs C10633). The filter and the QWP were removed. For nonlinear measurement, the incident power was the same as for the linear measurement, and an sCMOS camera (HAMAMATSU ORCA-Flash4.0 V3) was used to record the SH signal. For the measurement of nonlinear grayscale images, the QWP was removed to obtain signals with linear polarization.

Supporting Information

Supporting Information is available from the Wiley Online Library or from the author.

Acknowledgements

This work was supported by the National Key Research and Development Program of China (2021YFA1400601 and 2022YFA1404501), the National Natural Science Fund for Distinguished Young Scholar (11925403), and the National Natural Science Foundation of China (12122406, 12192253, 12104243, and U22A20258).

Conflict of Interest

The authors declare no conflicts of interest.

Data Availability Statement

The data that support the findings of this study are available in the supplementary material of this article.

Keywords

information encryption, Malus's law, metasurface, nonlinear optics, second harmonic generation

Received: September 5, 2023
Revised: January 5, 2024
Published online:

[1] N. Yu, P. Genevet, M. A. Kats, F. Aieta, J.-P. Tetienne, F. Capasso, Z. Gaburro, *Science* **2011**, *334*, 333.
[2] S. Sun, K. Y. Yang, C. M. Wang, T. K. Juan, W. T. Chen, C. Y. Liao, Q. He, S. Xiao, W. T. Kung, G. Y. Guo, L. Zhou, D. P. Tsai, *Nano Lett.* **2012**, *12*, 6223.
[3] L. Huang, X. Chen, H. Mühlenbernd, G. Li, B. Bai, Q. Tan, G. Jin, T. Zentgraf, S. Zhang, *Nano Lett.* **2012**, *12*, 5750.
[4] G. Li, L. Wu, K. F. Li, S. Chen, C. Schlickriede, Z. Xu, S. Huang, W. Li, Y. Liu, E. Y. B. Pun, T. Zentgraf, K. W. Cheah, Y. Luo, S. Zhang, *Nano Lett.* **2017**, *17*, 7974.
[5] Z. Li, W. Liu, Z. Li, C. Tang, H. Cheng, J. Li, X. Chen, S. Chen, J. Tian, *Laser Photonics Rev.* **2018**, *12*, 1800164.
[6] H. Ahmed, H. Kim, Y. Zhang, Y. Intaravanne, J. Jang, J. Rho, S. Chen, X. Chen, *Nanophotonics* **2022**, *11*, 941.
[7] X. Zhang, L. Huang, R. Zhao, H. Zhou, X. Li, G. Geng, J. Li, X. Li, Y. Wang, S. Zhang, *Sci. Adv.* **2022**, *8*, eabp8073.
[8] H. Zhou, B. Sain, Y. Wang, C. Schlickriede, R. Zhao, X. Zhang, Q. Wei, X. Li, L. Huang, T. Zentgraf, *ACS Nano* **2020**, *14*, 5553.
[9] X. Li, R. Zhao, Q. Wei, G. Geng, J. Li, S. Zhang, L. Huang, Y. Wang, *Adv. Funct. Mater.* **2021**, *31*, 2103326.
[10] Z. Li, W. Liu, H. Cheng, D. Y. Choi, S. Chen, J. Tian, *Adv. Mater.* **2020**, *32*, 1907983.
[11] R. Fu, K. Chen, Z. Li, S. Yu, G. Zheng, *Opto-Electron Sci* **2022**, *1*, 220011.
[12] K. T. P. Lim, H. Liu, Y. Liu, J. K. W. Yang, *Nat. Commun.* **2019**, *10*, 25.
[13] D. Wen, J. J. Cadusch, J. Meng, K. B. Crozier, *Adv. Funct. Mater.* **2020**, *30*, 1906415.
[14] F. Zhang, M. Pu, P. Gao, J. Jin, X. Li, Y. Guo, X. Ma, J. Luo, H. Yu, X. Luo, *Adv. Sci.* **2020**, *7*, 1903156.
[15] W. Yang, G. Qu, F. Lai, Y. Liu, Z. Ji, Y. Xu, Q. Song, J. Han, S. Xiao, *Adv. Mater.* **2021**, *33*, 2101258.
[16] S. M. Kamali, E. Arbabi, A. Arbabi, Y. Horie, M. Faraji-Dana, A. Faraon, *Phys. Rev. X* **2017**, *7*, 041056.
[17] S. Wan, C. Wan, C. Dai, Z. Li, J. Tang, G. Zheng, Z. Li, *Adv. Opt. Mater.* **2021**, *9*, 2101547.
[18] J. Guo, T. Wang, B. Quan, H. Zhao, C. Gu, J. Li, X. Wang, G. Situ, Y. Zhang, *Opto-Electron. Adv.* **2019**, *2*, 18002901.
[19] P. Zheng, Q. Dai, Z. Li, Z. Ye, J. Xiong, H.-C. Liu, G. Zheng, S. Zhang, *Sci. Adv.* **2021**, *7*, eabg0363.
[20] W. Wan, W. Yang, H. Feng, Y. Liu, Q. Gong, S. Xiao, Y. Li, *Adv. Opt. Mater.* **2021**, *9*, 2100626.
[21] Y. Cao, L. Tang, J. Li, C. Lee, Z.-G. Dong, *Nanophotonics* **2022**, *11*, 3365.
[22] Z. L. Deng, Q. A. Tu, Y. Wang, Z. Q. Wang, T. Shi, Z. Feng, X. C. Qiao, G. P. Wang, S. Xiao, X. Li, *Adv. Mater.* **2021**, *33*, 2103472.
[23] Q. Fan, M. Liu, C. Zhang, W. Zhu, Y. Wang, P. Lin, F. Yan, L. Chen, H. J. Lezec, Y. Lu, A. Agrawal, T. Xu, *Phys. Rev. Lett.* **2020**, *125*, 267402.
[24] Y. Zhou, I. I. Kravchenko, H. Wang, H. Zheng, G. Gu, J. Valentine, *Light: Sci. Appl.* **2019**, *8*, 80.
[25] Q. Dai, Z. Guan, S. Chang, L. Deng, J. Tao, Z. Li, Z. Li, S. Yu, G. Zheng, S. Zhang, *Adv. Funct. Mater.* **2020**, *30*, 2003990.
[26] W. Wan, W. Yang, S. Ye, X. Jiang, Y. Han, H. Feng, Y. Liu, Q. Gong, S. Xiao, Y. Li, *Adv. Opt. Mater.* **2022**, *10*, 2201478.
[27] N. Zhao, Z. Li, G. Zhu, J. Li, L. Deng, Q. Dai, W. Zhang, Z. He, G. Zheng, *Opt. Express* **2022**, *30*, 37554.
[28] F. Yue, C. Zhang, X.-F. Zang, D. Wen, B. D. Gerardot, S. Zhang, X. Chen, *Light: Sci. Appl.* **2018**, *7*, 17129.
[29] R. Zhao, X. Xiao, G. Geng, X. Li, J. Li, X. Li, Y. Wang, L. Huang, *Adv. Funct. Mater.* **2021**, *31*, 2100406.
[30] J. Deng, L. Deng, Z. Guan, J. Tao, G. Li, Z. Li, Z. Li, S. Yu, G. Zheng, *Nano Lett.* **2020**, *20*, 1830.
[31] L. Deng, J. Deng, Z. Guan, J. Tao, Y. Chen, Y. Yang, D. Zhang, J. Tang, Z. Li, Z. Li, S. Yu, G. Zheng, H. Xu, C.-W. Qiu, S. Zhang, *Light: Sci. Appl.* **2020**, *9*, 101.
[32] R. Ren, Z. Li, L. Deng, X. Shan, Q. Dai, Z. Guan, G. Zheng, S. Yu, *Nanophotonics* **2021**, *10*, 2903.
[33] Z. Li, C. Chen, Z. Guan, J. Tao, S. Chang, Q. Dai, Y. Xiao, Y. Cui, Y. Wang, S. Yu, G. Zheng, S. Zhang, *Laser Photonics Rev.* **2020**, *14*, 2000032.
[34] G. Li, S. Chen, N. Pholchai, B. Reineke, P. W. Wong, E. Y. Pun, K. W. Cheah, T. Zentgraf, S. Zhang, *Nat. Mater.* **2015**, *14*, 607.
[35] W. Ye, F. Zeuner, X. Li, B. Reineke, S. He, C. W. Qiu, J. Liu, Y. Wang, S. Zhang, T. Zentgraf, *Nat. Commun.* **2016**, *7*, 11930.
[36] B. Reineke, B. Sain, R. Zhao, L. Carletti, B. Liu, L. Huang, C. De Angelis, T. Zentgraf, *Nano Lett.* **2019**, *19*, 6585.
[37] M. Ma, Z. Li, W. Liu, C. Tang, Z. Li, H. Cheng, J. Li, S. Chen, J. Tian, *Laser Photonics Rev.* **2019**, *13*, 1900045.

[38] B. Liu, B. Sain, B. Reineke, R. Zhao, C. Meier, L. Huang, Y. Jiang, T. Zentgraf, *Adv. Opt. Mater.* **2020**, *8*, 1902050.
[39] J. Deng, Y. Tang, S. Chen, K. Li, A. V. Zayats, G. Li, *Nano Lett.* **2020**, *20*, 5421.
[40] T. Abir, M. Tal, T. Ellenbogen, *Nano Lett.* **2022**, *22*, 2712.
[41] Y. Li, G. Zhang, Y. Tang, X. Zhang, W. Cai, Y. Liu, T. Cao, G. Li, *Nanophotonics* **2022**, *11*, 2245.
[42] X. Zhang, L. He, X. Gan, X. Huang, Y. Du, Z. Zhai, Z. Li, Y. Zheng, X. Chen, Y. Cai, X. Ao, *Laser Photonics Rev.* **2022**, *16*, 2200031.
[43] Z. Hao, W. Liu, Z. Li, Z. Li, G. Geng, Y. Wang, H. Cheng, H. Ahmed, X. Chen, J. Li, J. Tian, S. Chen, *Laser Photonics Rev.* **2021**, *15*, 2100207.
[44] N. Segal, S. Keren-Zur, N. Hendler, T. Ellenbogen, *Nat. Photonics* **2015**, *9*, 180.
[45] X. Yang, C. Zhang, M. Wan, Z. Chen, Z. Wang, *Opt. Lett.* **2016**, *41*, 2938.
[46] W. Zang, Z. Qin, X. Yang, Z. Chen, S. Wang, Z. Wang, *Adv. Opt. Mater.* **2019**, *7*, 1801747.
[47] X. Zhang, J. Deng, M. Jin, Y. Li, N. Mao, Y. Tang, X. Liu, W. Cai, Y. Wang, K. Li, Y. Liu, G. Li, *Sci. China Phys. Mech.* **2021**, *64*, 294215.
[48] N. Ichiji, A. Kubo, *Opt. Lett.* **2022**, *47*, 265.
[49] C. Enkrich, M. Wegener, S. Linden, S. Burger, L. Zschiedrich, F. Schmidt, J. F. Zhou, T. Koschny, C. M. Soukoulis, *Phys. Rev. Lett.* **2005**, *95*, 203901.
[50] Y. Gao, Y. Fan, Y. Wang, W. Yang, Q. Song, S. Xiao, *Nano Lett.* **2018**, *18*, 8054.
[51] N. Mao, G. Zhang, Y. Tang, Y. Li, Z. Hu, X. Zhang, K. Li, K. Cheah, G. Li, *Proc. Natl. Acad. Sci* **2022**, *119*, e2204418119.
[52] Y. Jiang, W. Liu, Z. Li, D. Y. Choi, Y. Zhang, H. Cheng, J. Tian, S. Chen, *Adv. Opt. Mater.* **2023**, *11*, 2202186.
[53] C. Schlickriede, N. Waterman, B. Reineke, P. Georgi, G. Li, S. Zhang, T. Zentgraf, *Adv. Mater.* **2018**, *30*, 1703843.
[54] M. L. Tseng, M. Semmlinger, M. Zhang, C. Arndt, T. T. Huang, J. Yang, H. Y. Kuo, V. C. Su, M. K. Chen, C. H. Chu, B. Cerjan, D. P. Tsai, P. Nordlander, N. J. Halas, *Sci. Adv.* **2022**, *8*, eabn5644.
[55] N. Mao, J. Deng, X. Zhang, Y. Tang, M. Jin, Y. Li, X. Liu, K. Li, T. Cao, K. Cheah, H. Wang, J. Ng, G. Li, *Nano Lett.* **2020**, *20*, 7463.
[56] Y. Tang, Y. Intaravanne, J. Deng, K. F. Li, X. Chen, G. Li, *Phys. Rev. Appl.* **2019**, *12*, 024028.
[57] C. Ciracì, E. Poutrina, M. Scalora, D. R. Smith, *Phys. Rev. B* **2012**, *86*, 115451.
[58] E. D. Palik, *Handbook of Optical Constants of Solids*, Academic Press, New York **1998**.